



## LJMU Research Online

**Pitchford, WH, Kim, H-J, Ivanov, AP, Kim, H-M, Yu, J-S, Leatherbarrow, RJ, Albrecht, T, Kim, K-B and Edel, JB**

**Synchronized Optical and Electronic Detection of Biomolecules Using a Low Noise Nanopore Platform**

<http://researchonline.ljmu.ac.uk/id/eprint/8861/>

### Article

**Citation** (please note it is advisable to refer to the publisher's version if you intend to cite from this work)

**Pitchford, WH, Kim, H-J, Ivanov, AP, Kim, H-M, Yu, J-S, Leatherbarrow, RJ, Albrecht, T, Kim, K-B and Edel, JB (2015) Synchronized Optical and Electronic Detection of Biomolecules Using a Low Noise Nanopore Platform. ACS Nano. 9 (2). pp. 1740-1748. ISSN 1936-0851**

LJMU has developed [LJMU Research Online](#) for users to access the research output of the University more effectively. Copyright © and Moral Rights for the papers on this site are retained by the individual authors and/or other copyright owners. Users may download and/or print one copy of any article(s) in LJMU Research Online to facilitate their private study or for non-commercial research. You may not engage in further distribution of the material or use it for any profit-making activities or any commercial gain.

The version presented here may differ from the published version or from the version of the record. Please see the repository URL above for details on accessing the published version and note that access may require a subscription.

For more information please contact [researchonline@ljmu.ac.uk](mailto:researchonline@ljmu.ac.uk)

<http://researchonline.ljmu.ac.uk/>

# Synchronized Optical and Electronic Detection of Biomolecules using a Low Noise Nanopore Platform

*William H. Pitchford,<sup>#,†</sup> Hyung-Jun Kim<sup>#,‡</sup> Aleksandar P. Ivanov,<sup>†</sup> Hyun-Mi Kim,<sup>‡</sup> Jae-Seok Yu,<sup>‡</sup>  
Robin J. Leatherbarrow<sup>†</sup>, Tim Albrecht,<sup>\*,†</sup> Ki-Bum Kim,<sup>\*,‡</sup> Joshua B. Edel,<sup>\*,†</sup>*

<sup>†</sup>Department of Chemistry, Imperial College London, South Kensington Campus, London SW7 2AZ, UK

<sup>‡</sup>Department of Materials Science and Engineering, Seoul National University, Seoul 151-742, Korea

KEYWORDS: nanopore, single-molecule, fluorescence, noise, zero-mode waveguide

<sup>#</sup>Authors contributed equally

Corresponding Authors:

Joshua B. Edel [joshua.edel@imperial.ac.uk](mailto:joshua.edel@imperial.ac.uk)

Ki-Bum Kim [kibum@snu.ac.kr](mailto:kibum@snu.ac.kr)

Tim Albrecht [t.albrecht@imperial.ac.uk](mailto:t.albrecht@imperial.ac.uk)

**ABSTRACT** Inspired by the Coulter counter and molecular transport across biological pores, in the past two decades there has been a tremendous amount of research into the use of nanopores as single molecule sensors. Recently, the desire to increase structural resolution and analytical throughput has led to the integration of additional detection methods such as fluorescence spectroscopy. For structural information to be probed electronically high bandwidth measurements are crucial due to the high translocation velocity of molecules. The most commonly used solid-state nanopore sensors consist of a silicon nitride membrane and bulk silicon substrate. Unfortunately, the photo-induced noise associated with illumination of these platforms limits their applicability to high bandwidth, high laser power synchronized optical and electronic measurements. Here we present a unique low noise nanopore platform, composed of a predominately Pyrex substrate and silicon nitride membrane, for synchronized optical and electronic detection of biomolecules. Proof of principle experiments are conducted that show the Pyrex substrate substantially lowers ionic current noise arising from both laser illumination and platform capacitance. Furthermore, using confocal microscopy and a partially metallic pore we demonstrate high signal-to-noise synchronized optical and electronic detection of dsDNA.

Initially inspired by molecular transport across biological pores and the Coulter counter, the use of nanopores as single molecule sensors has come into prominence in the past two decades with a remarkable quantity of research having been published.<sup>1</sup> The most commonly used detection method is that of resistive pulse sensing, where analyte molecules are electrophoretically driven across an insulating membrane, separating two sides of an electrolyte, via a nanopore. Single-molecule detection is subsequently provided by the transient reduction in pore conductance from the steady-state whilst an analyte is present in the pore. Using this technique, a wide range of analytes have now been studied, most commonly single- and double-stranded DNA and proteins, with both biological and solid-state nanopores.<sup>2-5</sup>

Recently, the desire to acquire complementary information, increase structural resolution and analytical throughput has led to the integration of additional detection methods such as transverse electrodes and optical detection via Raman and fluorescence spectroscopy.<sup>6-9</sup> The integration of fluorescence spectroscopy is of particular value due to its versatility: a range of molecular properties can be probed including molecular distance (via FRET), orientation (via polarization) and local environment (via quenching).<sup>10</sup> In addition, the nanopore platform provides the potential to enhance optical detection via control of throughput, incorporation of additional photonic structure or use as a zero-mode waveguide.<sup>7,11</sup> A number of optical configurations have so far been reported, these include the use of wide-field imaging<sup>7</sup>, liquid core anti-resonant reflecting optical waveguides<sup>12</sup>, total internal reflection fluorescence microscopy<sup>13,14</sup> and confocal fluorescence microscopy.<sup>7</sup>

For structural information to be probed via resistive pulse sensing, high temporal resolution measurements are crucial due to the high translocation velocity of molecules. The most commonly used solid-state nanopore sensors consist of a silicon nitride membrane and bulk

silicon substrate.<sup>15</sup> Unfortunately, the high frequency noise, so-called dielectric noise, associated with these platforms high capacitance reduces the signal bandwidth at which molecules may be detected. Although integrated measurement electronics and additional dielectric layers can reduce background noise consequently increasing operating signal bandwidth<sup>16,17</sup>, an additional noise source exists under laser illumination due to the presence of Si.<sup>18</sup> This photo-induced noise significantly limits the applicability of these platforms to high bandwidth, high laser power simultaneous optical and electronic measurements.

Here we present a unique low noise nanopore platform, composed of a predominately pyrex substrate and silicon nitride membrane as a platform for the synchronized optical and electronic detection of biomolecules. Pyrex's high resistivity lowers device capacitance (~71 pF in 1M KCl buffer) and therefore high frequency noise enabling sub-5 pA RMS ionic current measurements at 10 kHz bandwidth. Furthermore, the absence of a bulk Si substrate means photoinduced increases of RMS current are typically sub-pA in magnitude.

The application of a confocal microscope to a hybrid nanopore-zero mode waveguide platform is perhaps the most powerful technique for directly probing a single nanopore due to localised excitation volumes on the order of a zeptolitre and single photon resolution.<sup>7,19</sup> For this technique, a partially metallic nanopore is crucial so that no propagation modes for incident light exist within the nanopore. Using platforms coated with aluminium, we demonstrate synchronized optical and electronic detection of biomolecule translocation events. Aluminium was chosen due to its high extinction coefficient and high reflectivity at the desired wavelength (488 nm).<sup>20</sup> This enabled the use of membranes composed of only 30 nm thick aluminium and 20 nm thick silicon nitride, therefore providing a small nanopore volume whilst also ensuring low transmittance of light across the pore and bulk membrane. We show signal-to-noise ratios of up to 15.6 are

possible for the optical detection of Yoyo-1 labelled 5 kbp DNA (7.5 base pairs to one dye molecule) within 0.1M KCl at a temporal resolution of 0.5 ms.

## Results and Discussion

A unique low noise nanopore platform was used in this study in order to mitigate photoinduced ionic current noise. This device is composed of a nanopore within a pyrex substrate based SiN<sub>x</sub> (Py-SiN<sub>x</sub>) platform (Figure 1A) instead of a typical Si substrate based SiN<sub>x</sub> (Si-SiN<sub>x</sub>) platform (Figure 1B). Both platform types were fabricated so that their photoinduced noise characteristics could be compared within a typical 0.1 M KCl electrolyte (Materials and Methods). The devices contained a 20 nm thick SiN<sub>x</sub> free standing membrane (Py-SiN<sub>x</sub>: 5 μm × 5 μm, Si-SiN<sub>x</sub>: 50 μm × 50 μm) into which 5-30 nm diameter nanopores were milled using a JEOL 2010F transmission electron microscope.

Simultaneous optical and electrical measurements were enabled by mounting nanopore devices in an optical cell, using a coverslip as a base. This enabled illumination of the nanopore using a custom-built confocal microscope (Figure 1E, Materials and Methods).<sup>21</sup> Briefly, nanopores were illuminated using an optical configuration employing a 488 nm continuous-wave solid-state laser (Sapphire 488LP, Coherent) and a 60x water immersion objective (1.20 NA, UPLSAPO 60XW, UIS2, Olympus). Fluorescence emission was split into two bands, 500-580 nm and 640-800 nm, before detection by two avalanche photodiodes and logged via a DAQ card at 100 kHz. A transmembrane potential was applied to nanopores using an A-M systems 2400 patch-clamp amplifier with Ag/AgCl electrodes. Unless otherwise stated the analogue signal was low pass filtered at 10 kHz before digitization at 100 kHz. Synchronised optical and electrical data

acquisition was enabled through the use of hardware and a custom LabView program for optical data acquisition (Figure 1E). Briefly, optical data acquisition using the Labview program was triggered by a TTL pulse, generated via a DAQ card once electrical data acquisition was initiated using Strathclyde Electrophysiology Software (WinWCP V4 8.4).

As a result of Pyrex's high resistivity ( $400 \text{ M}\Omega \text{ m}$ ), Py-SiN<sub>x</sub> platforms have lower capacitance ( $\sim 71 \text{ pF}$  in  $1 \text{ M KCl}$  buffer) and therefore exhibit lower dielectric and input capacitance noise than Si-SiN<sub>x</sub> platforms (Boron doped, Si substrate resistivity:  $1\text{-}30 \text{ }\Omega \text{ cm}$ ).<sup>22</sup> Consequently, with the laser turned off, the level of electrical noise for Py-SiN<sub>x</sub> platforms was lower than that for Si-SiN<sub>x</sub> platforms. For example, the standard deviation of ionic current at  $0 \text{ mV}$  bias, with the laser turned off, for a  $\sim 27 \text{ nm}$  diameter nanopore was only  $4.02 \pm 0.02 \text{ pA}$  for a Py-SiN<sub>x</sub> platform compared to  $26.9 \pm 0.9 \text{ pA}$  for a Si-SiN<sub>x</sub> platform. Furthermore, bypassing the low pass Bessel filter integrated within the amplifier, a Py-SiN<sub>x</sub> platform provides a standard deviation of only  $6.74 \text{ pA}$  at  $0 \text{ mV}$  bias. There is also a substantial difference in the response of the devices to laser illumination. Figure 2A shows the baseline ionic current at  $0 \text{ mV}$  bias for a nanopore within a Py-SiN<sub>x</sub> and Si-SiN<sub>x</sub> platform, as laser power is raised to  $580 \mu\text{W}$  in magnitude. Assuming a cylindrical geometry, the pores have an approximate diameter of  $27 \text{ nm}$  based on the measured pore conductance (Py-SiN<sub>x</sub> conductance:  $25.5 \text{ nS}$ , Si-SiN<sub>x</sub> conductance:  $25.4 \text{ nS}$ ).<sup>1</sup> The standard deviation of the ionic current standard increases by  $780.1 \pm 25.8 \text{ pA}$  ( $2864.2 \pm 95.1\%$ ) for the Si-SiN<sub>x</sub> platform compared to only  $0.9 \pm 0.1 \text{ pA}$  ( $17.6 \pm 1.4\%$ ) for the Py-SiN<sub>x</sub> platform (Figure S1, Supporting Information). Figure 2B and 2C show power spectrums densities (PSDs) for both platforms with the laser off and at  $\sim 580 \mu\text{W}$  laser power. Interestingly, a broad peak centred at  $\sim 225 \text{ Hz}$  exists at  $\sim 580 \mu\text{W}$  laser power for the Si-SiN<sub>x</sub> platform. Both photo-induced heating of the electrolyte and surface charge change for silicon nitride nanopores have previously been

reported.<sup>23,24</sup> However, the frequency dependence of this noise source is inconsistent with that of surface charge protonation noise or temperature dependant thermal and dielectric noise.<sup>22,25</sup>

Furthermore, this peaks absence within the Py-SiN<sub>x</sub> platforms power spectrum suggests the source of noise is related to the Si substrate. The optical transparency of the SiN<sub>x</sub> membrane and photon energy (2.54 eV) is sufficient for electron-hole pair generation in the Si substrate (band gap ~1.1 eV), reported to promote photoreduction of H<sup>+</sup> at p-type Si interfaces.<sup>26</sup> We therefore suspect, as previously reported, that the increase in noise is via electrochemical reaction at the silicon-electrolyte interface.<sup>18</sup>

The small increase of noise for Py-SiN<sub>x</sub> platforms stems from an increase in pore conductance with laser illumination and is a result of flicker noise scaling with the square of the ionic current and thermal noise being directly proportional to pore conductance.<sup>22,27</sup> Figure 3A shows current-voltage characteristics and corresponding conductance's at 0 mV bias for a ~7 nm diameter pore (conductance: 4.0 nS at 0 mV) at laser powers up to ~596 μW. Increases in noise for this nanopore are minor: sub-pA at 0mV, 100mV and 200mV bias across the entire laser power range (Figure 3B). The linear scaling of pore conductance with laser power may be a result of increases in pore surface charge and local heating of the electrolyte.<sup>23,28</sup> Previous studies suggest temperature change is likely to be small. For instance, the absorption coefficient of water for 488 nm wavelength light (0.0144 m<sup>-1</sup>) is significantly lower than for 1064 nm wavelength light (12 m<sup>-1</sup>) which has been reported to increase temperature at a rate of 20 K per mW. [4,9]

Furthermore, introduction and translocation of 5 kbp DNA (0.75 nM), using this nanopore, revealed a reduction of translocation frequency by 25.8 ± 1.5% and 60.4 ± 5.6% at ~74 μW and ~204 μW laser power respectively (Figure S2, Supporting Information). An increase in surface charge is expected to reduce translocation frequency due to higher electro-osmotic flow, whilst



the opposite trend is expected from local heating due to lower solution viscosity.<sup>23,29-31</sup> These findings suggest that increases in surface charge are the primary source of conductance change. By assuming changes in pore conductance were due to an increase in surface charge density alone, an expression which provided conductance as a function of laser power was derived and fit to the inset within Figure 3A (Supporting Information, Equation 3). This expression provided an estimate of 27.9 mC m<sup>-2</sup> for the surface charge density with the laser turned off and 20.0 mC m<sup>-2</sup> W<sup>-1</sup> for the rate of change of surface charge. Both values are in good agreement with literature.<sup>23,25</sup>

PSDs of the ionic current at 200 mV and 0 mV bias were fit with  $S_n(f) = Af^{-\alpha}$  and  $S_n(f) = B + Cf + Df^2$ , respectively, where  $f$  is frequency;  $A$  is the amplitude of flicker noise;  $B$  of white (thermal) noise;  $C$  of dielectric noise and  $D$  of input capacitance noise (Figure 3C).<sup>22,32</sup> As expected, this analysis revealed an increase in the amplitude of both flicker noise and white (thermal) noise with laser power (Figure S3, Supporting Information). Due to dielectric and input capacitance noise's dependence on frequency ( $\propto f$  and  $\propto f^2$  respectively), for these power spectrum analysis was conducted on ionic current data low pass filtered at 20 kHz to increase the fitting range and certainty of extracted parameters. No significant dependence of the amplitude of either dielectric or input capacitance noise on laser power was found (Figure S4, Supporting Information).

Increases in the amplitude of thermal noise ( $B$ ) are in line with conductance changes as predicted using a thermal noise model,  $B = 4k_B TG$ , where  $T$  is temperature and  $G$  pore conductance. For instance, at 596  $\mu$ W laser power the amplitude of thermal noise increased by 35%  $\pm$  9.1% and pore conductance increased by 25% (Figure 3a, inset). It is important to note

that closer scrutiny of the dependence of flicker noise amplitude on laser power reveals that surface charge change may not solely be responsible for changes in pore conductance. Previous studies have shown that nanopores which exhibit low flicker noise ( $<1 \text{ pA}^2/\text{Hz}$  at 1 Hz) are well described by Hooges relation,  $S_{\text{Flicker}} = aI^2/f$ , where the normalised noise amplitude ( $a$ ) is given by  $a=\alpha/N_c$  where  $N_c$  is the number of charge carriers and  $\alpha$  is the Hooge parameter.<sup>33–35</sup> Although, the Hooge relation was not verified for these nanopore platforms, for example using different ionic strength electrolytes<sup>17,33</sup>, low flicker noise was indeed exhibited at 200 mV bias ( $\sim 1 \text{ pA}^2/\text{Hz}$  at 1Hz for 596  $\mu\text{W}$  laser power). If surface charge increases with the power of laser illumination, the normalised noise amplitude ( $a$ ) should decrease with laser power due to an increase in the number of charge carriers. Surprisingly, the normalised noise amplitude ( $a$ ) is approximately constant across the laser power range with a mean of  $3.56 \pm 0.17 \times 10^{-7}$  (Figure S3, inset, Supplementary Information). This suggests that rises in the magnitude of flicker noise are not due to an increase in the number of charge carriers and compromises the principle of conductance change via surface charge change for this system. This conclusion is of course strongly hinged on the Hooge relation being obeyed for these platforms, future experiments will focus on verifying this. Regardless of the mechanism responsible for conductance change, the increase of only flicker and thermal noise indicates that the pyrex platform enables ionic current measurements at a noise floor defined by the magnitude of conductance change induced by laser illumination.

*Synchronised Detection.* The low light induced noise of Py-SiN<sub>x</sub> nanopore devices make them ideal for utilisation with confocal microscopy for synchronised optical and electronic detection of biomolecules. Previous studies have demonstrated the advantages of a hybrid nanopore-zero-mode waveguide platform: reduced background photon noise, the ability to

precisely localise a molecule within the optical probe volume and control of throughput.<sup>7,36</sup> This powerful technique involves illumination of a partially metallic nanopore where, crucially, the lateral dimensions of the nanopore mean no propagation modes exist for the incident light. As a result, light inside the aperture decays evanescently resulting in confined excitation volumes on the order of a zeptolitre ( $1 \times 10^{-21}$ ). It is important pore length is not increased substantially by a metallic layer, as changes in pore conductance induced by a translocating molecule are inversely proportional to pore length.<sup>37</sup> Thus Py-SiN<sub>x</sub> platforms were coated with 30 nm thick aluminium via electron beam evaporation before milling of a sub-30 nm diameter pore. This structure was selected as it provided a small nanopore volume whilst also ensuring low transmittance of light across the pore and bulk membrane. Transmittance of light across the bulk membrane is significantly attenuated, with a reduction in the electromagnetic field intensity across a 30 nm thick Al membrane of ~20 dB ( $10 \log_{10} |E|^2$ ).<sup>20</sup> Furthermore, at the wavelength of interest (488 nm), the ZMW cut-off diameter is 215 nm ensuring attenuation of light intensity along the pore-axis.<sup>20</sup> Assuming the ZMW was fabricated using a perfect conductor, the intensity of light decays according to the below expression where  $h$  is pore depth,  $I_h$  is intensity at depth  $h$ ,  $I_o$  is initial intensity,  $\lambda_c$  is the cut-off wavelength and  $\lambda_m$  is the wavelength of incident light.<sup>38</sup> Using this equation, a reduction of intensity by 99.6% is expected at a depth of 5 nm within a 10 nm diameter pore. It should be noted that this only an estimate as attenuation is lower for real metals, due to a finite skin depth.<sup>39</sup>

$$\frac{I_h}{I_o} = \exp\left(-\frac{4\pi h}{\lambda_b} \sqrt{\left(\frac{\lambda_m}{\lambda_c}\right)^2 - 1}\right)$$

Before attempting synchronised detection, independent optical and electronic measurements of the translocation of 5kbp DNA were conducted to assess the viability of this platform for single molecule detection. Excellent signal-to-noise for both electronic and optical signals was provided by these nanopore platforms. Figure 4A shows a typical ionic current trace for a ~19 nm diameter nanopore (conductance: 49.6 nS) within a 1M KCl electrolyte, after introduction of 5 kbp DNA (2.6 nM) and application of a 100 mV bias. Corresponding event durations and amplitudes were extracted and are shown by a contour plot in figure 4B. Translocation events of linear and folded DNA molecules are easily distinguished and are labelled as type 1 and 2 events respectively.<sup>3</sup>

For optical detection, DNA was labelled with Yoyo-1 at ratio of 7.5 base pairs to one dye molecule. Yoyo<sup>®</sup>-1 was selected as its absorbance maximum (491 nm) is close to the wavelength of the laser (488 nm). The fluorescence of Yoyo<sup>®</sup>-1 is quenched by chloride ions, however a 0.1M KCl electrolyte provided good signal-to-noise with this binding ratio. Figure 4C shows an example optical trace for 500-580 nm wavelength fluorescence at 200 mV bias and ~17 $\mu$ W laser power illumination, after the introduction of labelled DNA (0.85 nM) to a 30 nm diameter pore (conductance: 25.7 nS). The presence of a translocating DNA molecule within the optical probe volume results in a burst of fluorescence. Corresponding dwell times and event amplitudes were extracted, using a custom Matlab script, and are shown within a contour plot in figure 4D. Signal-to-noise is excellent: the ratio of mean pulse height ( $28.5 \pm 11.6$  photons per 0.5 ms) to background photon counts ( $1.85 \pm 0.65$  photons per 0.5 ms) is  $15.6 \pm 8.3$ . The dwell time within the optical channel is larger than that would be expected in the electronic channel. A fit of a log-normal probability distribution function to a histogram of event duration provided a mean of  $78.3 \pm 3.9$  ms. This is a result of a molecule which has left the nanopore being detected

optically until it has left the focal plane via a combination of diffusion and electrokinetic phenomena.<sup>7</sup>

Synchronised optical and electrical data acquisition was enabled through the use of hardware and a custom LabView program for optical data acquisition (Figure 1B). Synchronization of optical and electrical signals was verified by illuminating a ~14 nm diameter nanopore (conductance: 9.1 nS) with 1.87 mW laser power in finite intervals using an optical beam shutter (Thorlabs, SHO5). Photoinduced increases in pore conductance were correlated with an increase of background fluorescence from the pore surface, detected within the red channel of the optical set-up ( $\lambda \sim 640\text{-}800\text{ nm}$ ). Cross-correlation of the two signals was conducted, for a total of 14 pulses, to quantify any delay in acquisition. This indicated that the electronic signal trailed the optical signal by an average of  $0.18 \pm 0.02\text{ ms}$  (Figure S5, Supporting Information). This delay is close to the difference in rise-time of the two signals,  $0.17 \pm 0.08\text{ ms}$ , indicating that data acquisition was indeed synchronized.

To demonstrate synchronised detection, we introduced Yoyo-1 labelled 5kbp DNA (0.790 nM) to a platform containing two pores (~10 nm and ~6 nm diameter, total conductance: 9.1 nS). Figure 5A shows a sample of the recorded ionic current ( $I(t)$ ) and optical fluorescence ( $F(t)$ ) signals at  $\sim 16\mu\text{W}$  laser power and -400 mV applied bias. A total of 191 events were detected in the optical channel and 206 events in the electronic channel: a 92.7% synchronized detection efficiency. The slightly lower quantity of events in the optical channel is in part due to the longer dwell time of DNA within the optical detection volume resulting in amalgamation of consecutive translocation events. Accounting for such events provides an efficiency of 93.7%. Efficiency could be improved further by using an alternate fluorescent dye, for example Alexa Fluor 488

whose fluorescence is not quenched by halides, this was deemed unnecessary for this proof of principle experiment.

Interestingly, an increase in ionic current upon exit of a DNA molecule from the pore is observed in 77.7% of events (160 events). This phenomenon was also observed for Py-SiN<sub>x</sub> platforms which contained a single nanopore, with and without Al (data not shown). Resistive pulses are a result of a decrease in the flux of ions across the pore and consequently pore conductance whilst a molecule is present. The mechanism responsible for a peak in ionic current (mean duration:  $0.08 \pm 0.03$  ms, mean amplitude:  $197.0 \pm 37.9$  pA) is less clear. If the diameter of the nanopore is close to that of dsDNA (2.2 nm) and its double layer ( $\lambda_D = 0.97$  nm for 0.1M KCl), this phenomenon can arise due to the release of accumulated electrolyte ions at the pore entrance after translocation and analyte double layer effects such as diffusive currents and concentration polarisation.<sup>40-42</sup> However, the nanopore dimensions (~10 nm and ~6 nm) are larger than that of a single DNA molecule and hence these mechanisms are unlikely to be significant. Instead, we suspect this peak in ionic current arises from electrostatic enhancement of counter-ion concentration at the pore exit due to molecule surface charge.<sup>43</sup> Menestrina *et al* have previously reported a decrease and subsequent increase in current upon entry and exit of negatively charged 410 nm diameter PMMA particles across a 1400 nm diameter pore for electrolyte concentrations <200mM KCl.<sup>43</sup> We believe that the peak in ionic current arises predominately due to this mechanism. We are not fully certain why this phenomenon is only observed in 77.7 % of events, but this may be a consequence of differing conformations of DNA upon leaving the pore.

A histogram of resistive pulse height revealed a single cluster of events with a mean amplitude of  $196.4 \pm 67.8$  pA (Figure 5C, inset). The corresponding molecule diameter was

estimated, neglecting surface charge effects, using the expression derived by Smeets *et al* as  $4.57 \pm 1.41$  nm.<sup>37</sup> This indicates that molecules translocated predominately in a folded conformation. A histogram of the resistive pulse duration, shown in figure 5b, was fit with the 1D linear translocation probability density function reported by Ling *et al*,  $F1(t) = (L/(4\pi Dt^3))^{1/2} e^{-(L-vt)^2/4Dt}$ , where  $v$  is drift velocity,  $L$  is the length of 5 kbp dsDNA and  $D$  is the diffusion coefficient.<sup>44</sup> The length of unfolded 5 kbp DNA is  $1.7 \mu\text{m}$ ; the Ling distribution indicated a molecule length of  $1.064 \mu\text{m}$  confirming that molecules were folded during translocation. The mean translocation time and drift velocity were  $0.283$  ms and  $3.76$  mm/s, which are in good agreement with literature.<sup>3,15</sup>

Synchronisation was verified by calculating the cross-correlation of  $I(t)$  and  $F(t)$  over a 84.6 second sample containing 84 translocation events. Cross-correlation yielded a single peak and showed that molecules were detected electronically first, with a delay of  $90 \mu\text{s}$  before optical detection (Figure 5E). This lag is close to the mean duration of the peaks in ionic current associated with the exit of molecules from the pore ( $0.08 \pm 0.03$  ms) and is a result of the evanescent decay of incident light along the pore axes. The delay in detection indicates that the effective optical observation volume is indeed confined to the far region of the pore.

## Conclusion

We have demonstrated synchronised optical and electronic detection of biomolecules using a unique low noise nanopore platform. The presence of a Pyrex substrate substantially lowers ionic current noise arising from both laser illumination and platform capacitance. Moreover, the use of a partially metallic pore as a zero-mode waveguide provides excellent optical signal-to-noise due

to a reduction of background photon noise and the ability to precisely localise a molecule within the probe volume.

This platform provides scope for high bandwidth and high laser power synchronised optical and electrical detection of biomolecules. This has an array of potential applications such as probing the translocation mechanism, enhanced conformational analysis (e.g. via single-particle FRET) and superior analyte discrimination within complex solutions. Furthermore, functionality could be enhanced by incorporation of appropriate photonic structure for control of local temperature, via plasmonic heating, and enable single molecule thermodynamic and kinetic biophysical studies.<sup>31,45</sup> For example, one can envisage experiments involving the modulation of temperature and subsequent probing of structural dynamics using electronic and optical detection. Ultimately, the application of these low noise platforms to synchronised optical and electronic detection enhances nanopore sensitivity and increases both the range of molecules which can be studied and potential applications of these sensors.

**Materials and Methods** Silicon substrate based silicon nitride (Si-SiN<sub>x</sub>) devices were fabricated from boron doped, <100> crystal orientation, 500 μm thick silicon wafers coated with 20 nm thick low-stress silicon nitride (SiN<sub>x</sub>). Briefly, wafers were segmented via photolithography and reactive ion etching (RIE) into 10mm x 10 mm chips, each with a central square window of SiN<sub>x</sub> removed. A wet KOH etch was subsequently used to establish a ~50 μm x 50 μm free standing SiN<sub>x</sub> membrane before milling of a nanopore using a JEOL 2010F transmission electron microscope.

Pyrex substrate based silicon nitride (Py-SiN<sub>x</sub>) devices were fabricated as follows. Pyrex substrates (10 mm x 10 mm, 200 μm thick) were coated with amorphous Si (a-Si, 200 nm thick)



on both sides via low pressure chemical vapour deposition. Photolithography and RIE were used to ‘open’ a  $5\ \mu\text{m} \times 5\ \mu\text{m}$  window in *a*-Si on the topside of the wafer before a HF wet etch (49 wt.%, 5 minutes) of the exposed pyrex. Photolithography and RIE were then used to define a  $100\ \mu\text{m} \times 100\ \mu\text{m}$  opening in *a*-Si on the bottom side of the wafer and a HF wet etch (49 wt.%) of the exposed pyrex used to merge the two etched chambers.  $\text{SiN}_x$  membranes (20 nm thick) were prepared separately via plasma-enhanced chemical vapour deposition onto a Ni-Si platform. Poly(methyl methacrylate) (PMMA, 200 nm thick) was then deposited via spin coating, yielding a PMMA/ $\text{SiN}_x$ /Ni/Si structure. Addition to a  $\text{FeCl}_3$  solution dissolved the Ni present, establishing a PMMA/ $\text{SiN}_x$  membrane which was added to the topside of the Py- $\text{SiN}_x$  platform. PMMA was subsequently dissolved using acetone and the  $\text{SiN}_x$  membrane secured by depositing photodefinable PDMS (10-20  $\mu\text{m}$  thick).<sup>46</sup> For synchronised detection using a zero-mode waveguide modality, a 30 nm thick aluminium layer was deposited onto the topside of the Py- $\text{SiN}_x$  platform (Py- $\text{SiN}_x$ -Al) via electron beam evaporation before deposition of PDMS.

All experiments were conducted using a reported custom-built confocal microscope.<sup>47</sup> Nanopores were illuminated using a 488 nm continuous-wave solid-state laser (Sapphire 488LP, Coherent) and a 60x water immersion objective (1.20 NA, UPLSAPO 60XW, UIS2, Olympus). Fluorescence emission was split into two bands, 500-580 nm and 640-800 nm, using a dichroic mirror (630DCXR) before detection by two avalanche photodiodes (SPCM-AQR-14, Perkin-Elmer) coupled with a DAQ card (NI 6602, National Instruments) for data logging. A transmembrane potential was applied to nanopore sensors using an A-M systems 2400 patch-clamp amplifier and Ag/AgCl electrodes. Unless otherwise stated, the analogue signal was filtered by an integrated 6 position, four pole low pass Bessel filter at 10 kHz before digitization

at 100 kHz using a NI-USB 6259 DAQ card. All electrolytes were buffered using 10mM Tris.HCl, 1mM EDTA (pH7).

Custom Matlab scripts were used for data analysis. Power spectrums were estimated, using a fast-fourier transform and 9.75 s duration data sets. To rectify signal attenuation before the cut-off frequency, power spectrums were normalised by the magnitude response of a four-pole low pass Bessel filter at the corresponding low pass filter frequency.<sup>47</sup> RMS current was calculated using 0.2 s ionic current traces.

Peak selection criteria for both optical and electrical translocation data was a minimum amplitude of 5 standard deviations of the background signal. To account for ionic current noise, the baseline of all electrical data was smoothed using an asymmetric least squares smoothing algorithm before peak selection.<sup>48</sup>

## **Acknowledgments**

This work was supported in part by an ERC starting investigator grant (J.B.E.) and a BBSRC grant.

**Conflict of Interest:** The authors declare no competing financial interest.

**Supporting Information:** Supporting Figures (Fig. S1-S5) mentioned in the main text are available online. This material is available free of charge via the Internet at <http://pubs.acs.org>.

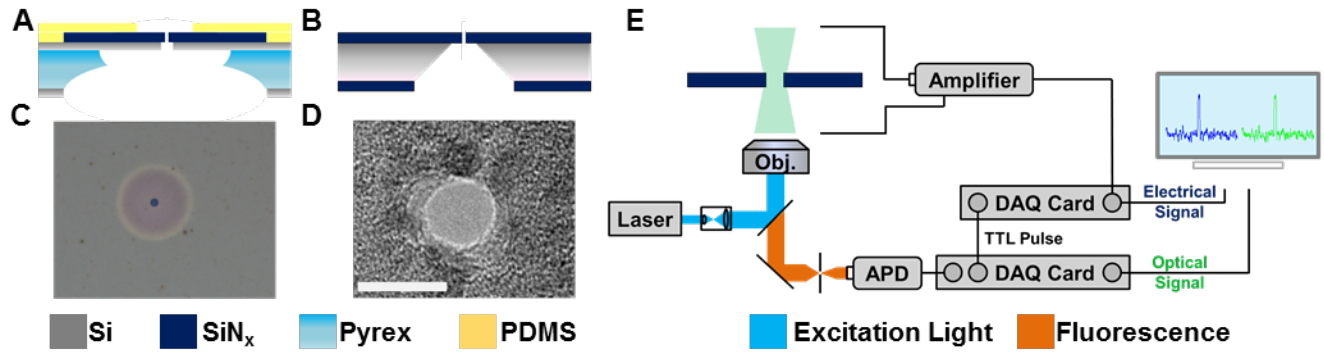


**Figure 1.** Schematics of A) Si and B) Pyrex substrate based silicon nitride nanopore platforms. C) Optical image of a Pyrex substrate (Py-SiN<sub>x</sub>) platform (scale bar = 10 μm). Two circular features are present. The larger feature (diameter: ~19 μm) corresponds to the aperture within the pyrex substrate and the smaller feature (diameter: ~2.1 μm) to the free standing silicon nitride membrane. D) TEM image of a ~7 nm diameter nanopore within the free-standing silicon nitride membrane of a Py-SiN<sub>x</sub> platform (scale bar = 10 nm). E) The experimental set-up: an epifluorescence optical configuration employing a 488 nm continuous-wave laser; a 60x water immersion objective (Obj.) and avalanche photodiode (APD) is used to probe a SiN<sub>x</sub> nanopore (Materials and Methods). When electrical data acquisition is initiated, a TTL pulse is generated by the electrical data acquisition (DAQ) card which subsequently triggers optical acquisition.

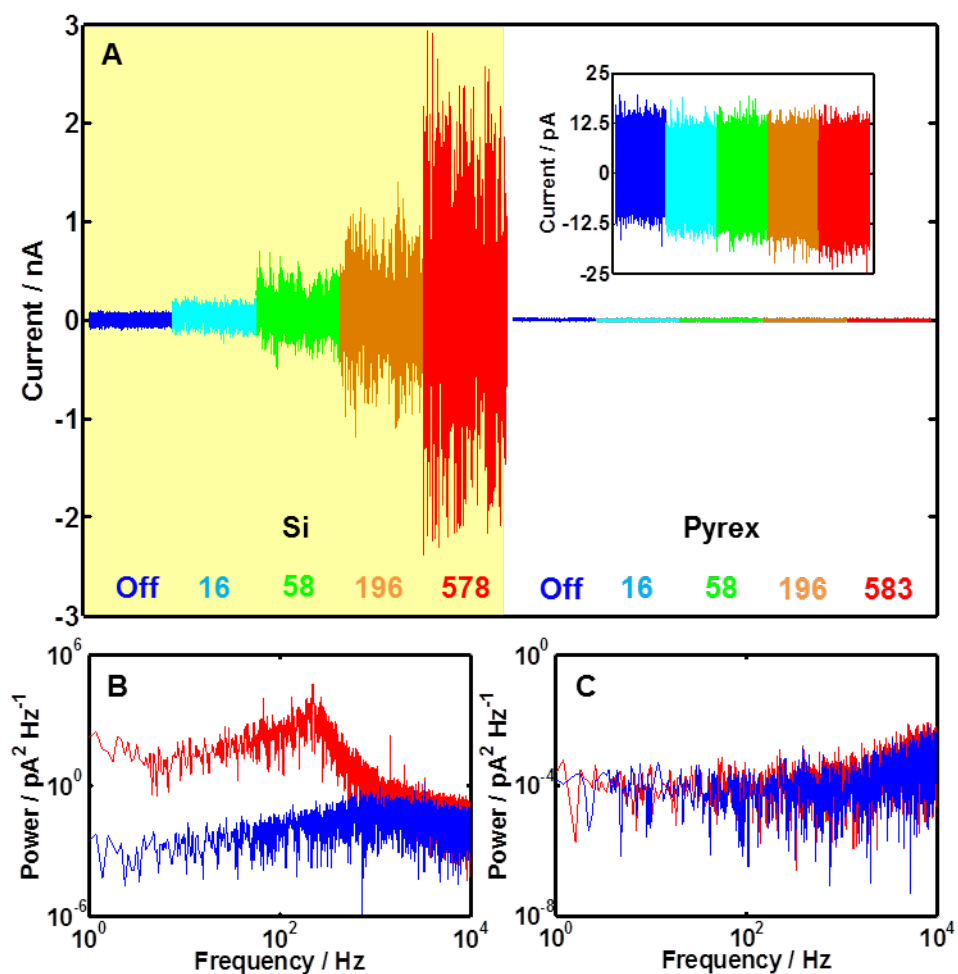


**Figure 2.** A) Baseline ionic current at 0 mV, under laser illumination, for a  $\sim 27$  nm diameter nanopore in a Si-SiN<sub>x</sub> (yellow background) and Py-SiN<sub>x</sub> platform. Different colour traces correspond to different laser powers, as indicated by the number (in  $\mu$ W units) beneath each trace. The inset is an expanded view of data for the Py-SiN<sub>x</sub> device. B) Power Spectral Densities at 0mV for the Si-SiN<sub>x</sub> platform with the laser off (blue) and at  $\sim 578$   $\mu$ W laser power (red). C) Power Spectral Densities at 0mV for the Py-SiN<sub>x</sub> platform with the laser off (blue) and at  $\sim 583$   $\mu$ W laser power (red).

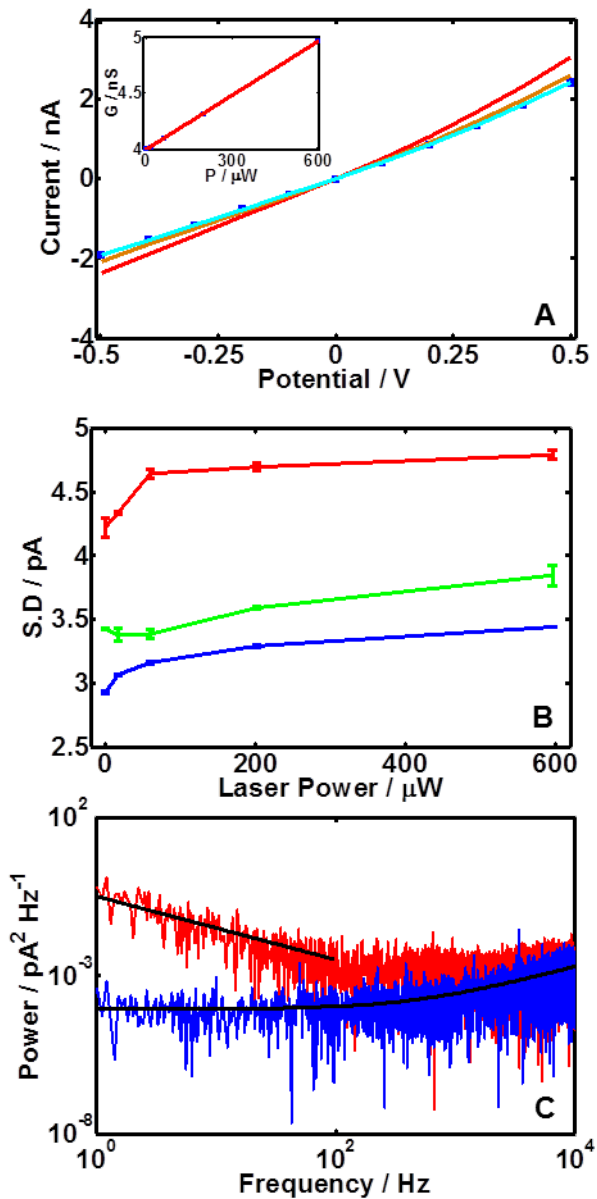


**Figure 3.** A) Current–Voltage trace for a  $\sim 7$  nm diameter (conductance: 4.0 nS at 0 mV) Py-SiN<sub>x</sub> nanopore with the laser off (blue) and at  $\sim 17 \mu\text{W}$  (blue),  $\sim 201 \mu\text{W}$  (orange) and  $\sim 596 \mu\text{W}$  (red) power. The inset shows pore conductance at 0 mV as a function of laser power. B) Standard deviation of ionic current versus laser power with a bias of 0mV (blue), -100mV (green) and -

200mV (red). C) Power Spectral Densities at 0 mV (blue) & -200mV (red) with the laser power at  $\sim 596 \mu\text{W}$ . Black lines indicate fits of  $S(f) = Af^\alpha$  and  $S(f) = B + Cf + Df^2$  (where  $A$ – $D$  are fitting parameters and  $0 < \alpha < 2$ , with exponent  $\alpha$  typically close to 1) for data collected at -200mV and 0mV respectively.

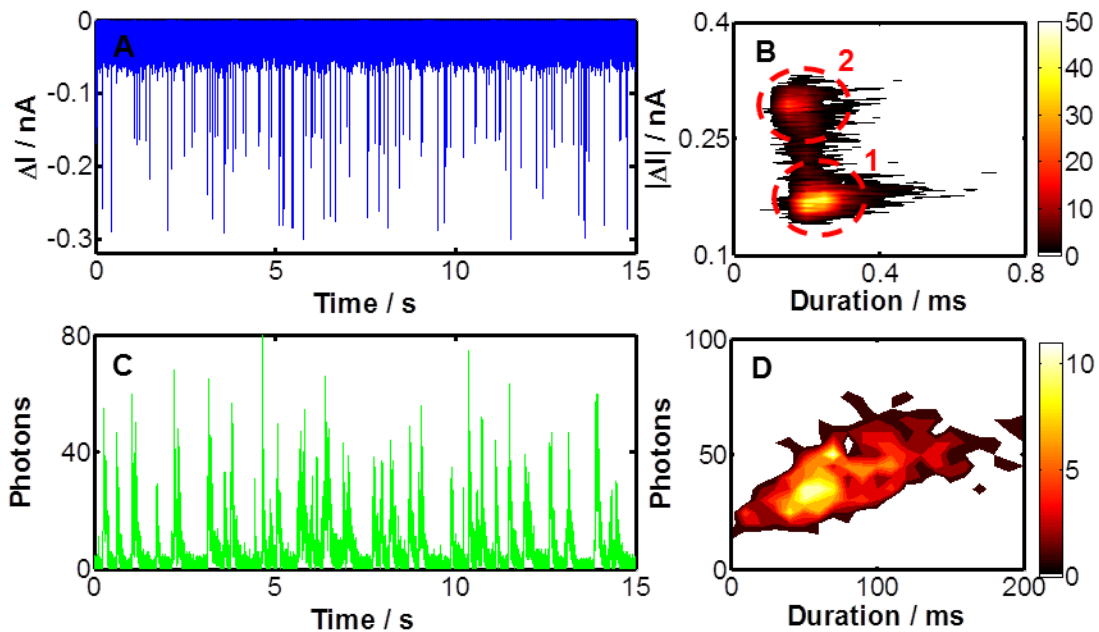


**Figure 4.** A) Baseline-adjusted ionic current trace for electrical 5 kbp DNA translocation detection at 100 mV using a  $\sim 19$  nm diameter pore (conductance: 49.6 nS) and 1M KCl electrolyte. B) Corresponding contour plot of event amplitude versus duration for 100 mV electrical detection data. C) Photon trace (0.5 ms resolution) for optical Yoyo<sup>®</sup>-1 labelled 5 kbp DNA (7.5bp's : 1 dye) translocation detection at 200 mV bias and  $\sim 17 \mu\text{W}$  laser power using a 30 nm diameter pore (conductance: 25.7 nS) and 0.1 M KCl electrolyte. Data corresponds to 500-580 nm wavelength fluorescence. D) Corresponding contour plot of event amplitude (photons per 0.5ms) versus duration for 200 mV optical detection data.

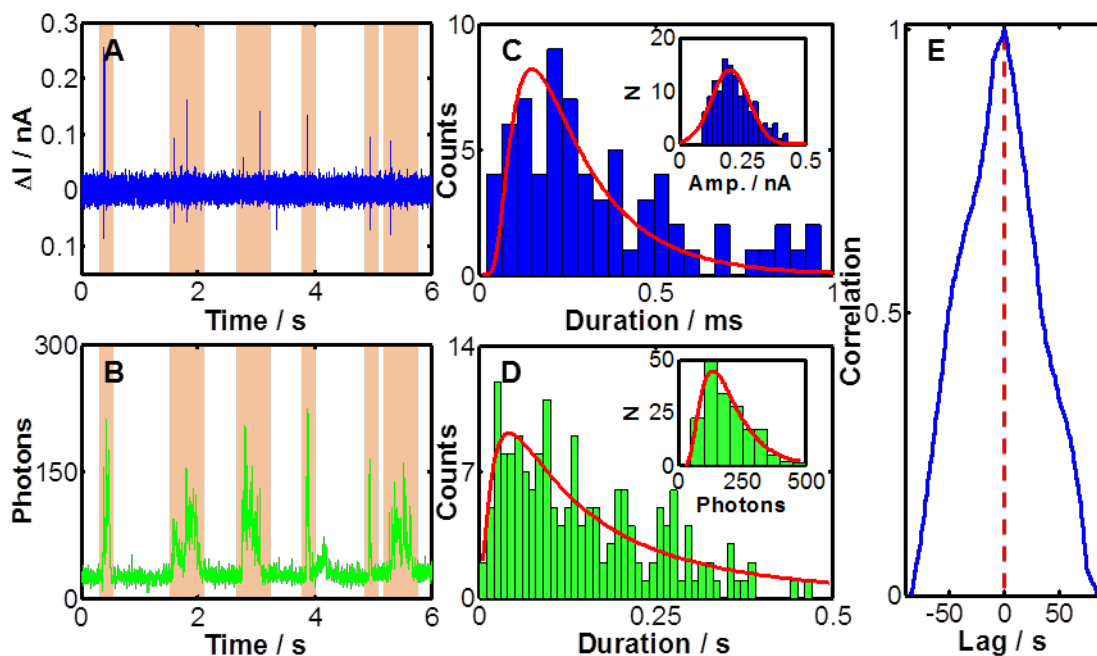
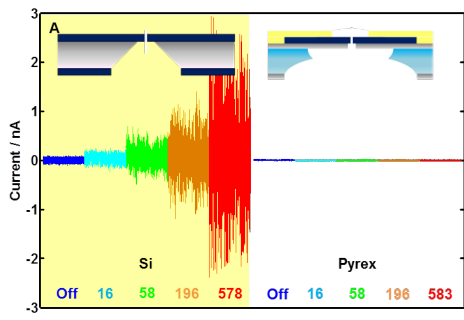


**Figure 5.** A) and B) Baseline adjusted ionic current and photon trace for Yoyo<sup>®</sup>-1 labelled 5 kbp DNA (7.5bp's : 1 dye) translocation detection at 400 mV bias and  $\sim 17 \mu\text{W}$  laser power using two pores ( $\sim 10$  nm and 6 nm diameter, total conductance: 9.1 nS) and a 0.1 M KCl electrolyte. Data within the optical channel has been re-binned at 2 ms resolution. B) Corresponding electrical data histograms of event duration and amplitude (inset) fit with Ling *et al* and Gaussian probability distribution functions, respectively.<sup>44</sup> C) Corresponding optical data histograms of event duration and amplitude (inset) fit with log-normal probability distribution functions. D) Cross-correlation of ionic current and photon counts within the green channel ( $\lambda \sim 500$ - 580 nm) for a 84.6 second sample containing 84 translocation events.



# TOC Image



## References

1. Wanunu, M. Nanopores: A Journey towards DNA Sequencing. *Phys. Life Rev.* **2012**, *9*, 125–158.
2. Fologea, D.; Gershow, M.; Ledden, B.; McNabb, D. S.; Golovchenko, J. A.; Li, J. Detecting Single Stranded DNA with a Solid State Nanopore. *Nano Lett.* **2005**, *5*, 1905–1909.
3. Storm, A. J.; Chen, J. H.; Zandbergen, H. W.; Dekker, C. Translocation of Double-Strand DNA through a Silicon Oxide Nanopore. *Phys. Rev. Stat. nonlinear, soft matter Phys.* **2005**, *71*, 51903.
4. Fologea, D.; Ledden, B.; McNabb, D. S.; Li, J. L. Electrical Characterization of Protein Molecules by a Solid-State Nanopore. *Appl. Phys. Lett.* **2007**, *91*.
5. Bayley, H.; Cremer, P. S. Stochastic Sensors Inspired by Biology. *Nature* **2001**, *413*, 226–230.
6. Ivanov, A. P.; Instuli, E.; McGilvery, C. M.; Baldwin, G.; McComb, D. W.; Albrecht, T.; Edel, J. B. DNA Tunneling Detector Embedded in a Nanopore. *Nano Lett.* **2011**, *11*, 279–285.
7. Chansin, G. A. T.; Mulero, R.; Hong, J.; Kim, M. J.; deMello, A. J.; Edel, J. B. Single-Molecule Spectroscopy Using Nanoporous Membranes. *Nano Lett.* **2007**, *7*, 2901–2906.
8. Cecchini, M. P.; Wiener, A.; Turek, V. A.; Chon, H.; Lee, S.; Ivanov, A. P.; McComb, D. W.; Choo, J.; Albrecht, T.; Maier, S. A.; *et al.* Rapid Ultrasensitive Single Particle Surface-Enhanced Raman Spectroscopy Using Metallic Nanopores. *Nano Lett.* **2013**, *13*, 4602–4609.

9. Miles, B. N.; Ivanov, A. P.; Wilson, K. A.; Dogan, F.; Japrun, D.; Edel, J. B. Single Molecule Sensing with Solid-State Nanopores: Novel Materials Methods and Applications. *Chem. Soc. Rev.* **2013**, *42*, 15–28.
10. Deniz, A. a; Mukhopadhyay, S.; Lemke, E. a. Single-Molecule Biophysics: At the Interface of Biology, Physics and Chemistry. *J. R. Soc. Interface* **2008**, *5*, 15–45.
11. Aouani, H.; Mahboub, O.; Bonod, N.; Devaux, E.; Popov, E.; Rigneault, H.; Ebbesen, T. W.; Wenger, J. Bright Unidirectional Fluorescence Emission of Molecules in a Nanoaperture with Plasmonic Corrugations. *Nano Lett.* **2011**, *11*, 637–644.
12. Liu, S.; Zhao, Y.; Parks, J. W.; Deamer, D. W.; Hawkins, A. R.; Schmidt, H. Correlated Electrical and Optical Analysis of Single Nanoparticles and Biomolecules on a Nanopore-Gated Optofluidic Chip. *Nano Lett.* **2014**, *14*, 4816–4820.
13. Soni, G. V; Singer, A.; Yu, Z.; Sun, Y.; McNally, B.; Meller, A. Synchronous Optical and Electrical Detection of Biomolecules Traversing through Solid-State Nanopores. *Rev. Sci. Instrum.* **2010**, *81*, 014301.
14. McNally, B.; Singer, A.; Yu, Z.; Sun, Y.; Weng, Z.; Meller, A. Optical Recognition of Converted DNA Nucleotides for Single-Molecule DNA Sequencing Using Nanopore Arrays. *Nano Lett.* **2010**, *10*, 2237–2244.
15. Li, J.; Gershow, M.; Stein, D.; Brandin, E.; Golovchenko, J. A. DNA Molecules and Configurations in a Solid-State Nanopore Microscope. *Nat. Mater.* **2003**, *2*, 611–615.

16. Rosenstein, J. K.; Wanunu, M.; Merchant, C. a; Drndic, M.; Shepard, K. L. Integrated Nanopore Sensing Platform with Sub-Microsecond Temporal Resolution. *Nat. Methods* **2012**, *9*, 487–492.
17. Vincent Tabard-Cossa, et al. Noise Analysis and Reduction in Solid-State Nanopores. *Nanotechnology*, **2007**, *18*, 305505.
18. Li, Y.; Chen, C.; Kerman, S.; Neutens, P.; Lagae, L.; Groeseneken, G.; Stakenborg, T.; Van Dorpe, P. Harnessing Plasmon-Induced Ionic Noise in Metallic Nanopores. *Nano Lett.* **2013**, *13*, 1724–1729.
19. Larkin, J.; Foquet, M.; Turner, S. W.; Korlach, J.; Wanunu, M. Reversible Positioning of Single Molecules inside Zero-Mode Waveguides. *Nano Lett.* **2014**, *14*, 6023–6029.
20. Hong, J.; Lee, Y.; Chansin, G. A. T.; Edel, J. B.; deMello, A. J. Design of a Solid-State Nanopore-Based Platform for Single-Molecule Spectroscopy. *Nanotechnology* **2008**, *19*, 165205.
21. Huebner, A.; Srisa-Art, M.; Holt, D.; Abell, C.; Hollfelder, F.; DeMello, A. J.; Edel, J. B. Quantitative Detection of Protein Expression in Single Cells Using Droplet Microfluidics. *Chem. Commun.* **2007**, 1218–1220.
22. Tabard-Cossa, V. Instrumentation for Low-Noise High-Bandwidth Nanopore Recording. In *Engineered Nanopores for Bioanalytical Applications*; Edel, J. B.; Albrecht, T., Eds.; Micro and Nano Technologies; William Andrew Publishing: Oxford, 2013; pp. 59–93.
23. Di Fiori, N.; Squires, A.; Bar, D.; Gilboa, T.; Moustakas, T. D.; Meller, A. Optoelectronic Control of Surface Charge and Translocation Dynamics in Solid-State Nanopores. *Nat. Nanotechnol.* **2013**, *8*, 946–951.

24. Keyser, U. F.; Krapf, D.; Koeleman, B. N.; Smeets, R. M. M.; Dekker, N. H.; Dekker, C. Nanopore Tomography of a Laser Focus. *Nano Lett.* **2005**, *5*, 2253–2256.
25. Hoogerheide, D. P.; Garaj, S.; Golovchenko, J. A. Probing Surface Charge Fluctuations with Solid-State Nanopores. *Phys. Rev. Lett.* **2009**, *102*, 256804.
26. Mathews, N. R.; Sebastian, P. J.; Mathew, X.; Agarwal, V. Photoelectrochemical Characterization of Porous Si. **2003**, *28*, 629–632.
27. Chen, P.; Mitsui, T.; Farmer, D. B.; Golovchenko, J.; Gordon, R. G.; Branton, D. Atomic Layer Deposition to Fine-Tune the Surface Properties and Diameters of Fabricated Nanopores. *Nano Lett.* **2004**, *4*, 1333–1337.
28. Keyser, U. F.; Krapf, D.; Koeleman, B. N.; Smeets, R. M. M.; Dekker, N. H.; Dekker, C. Nanopore Tomography of a Laser Focus. *Nano Lett.* **2005**, *5*, 2253–2256.
29. Meller, A.; Nivon, L.; Brandin, E.; Golovchenko, J.; Branton, D. Rapid Nanopore Discrimination between Single Polynucleotide Molecules. *Proc. Natl. Acad. Sci. U. S. A.* **2000**, *97*, 1079–1084.
30. Fologea, D.; Uplinger, J.; Thomas, B.; McNabb, D. S.; Li, J. Slowing DNA Translocation in a Solid-State Nanopore. *Nano Lett.* **2005**, *5*, 1734–1737.
31. Reiner, J. E.; Robertson, J. W. F.; Burden, D. L.; Burden, L. K.; Balijepalli, A.; Kasianowicz, J. J. Temperature Sculpting in Yoctoliter Volumes. *J. Am. Chem. Soc.* **2013**, *135*, 3087–3094.

32. Levis, R. A.; Rae, J. L. The Use of Quartz Patch Pipettes for Low Noise Single Channel Recording. *Biophys. J.* **1993**, *65*, 1666–1677.
33. Smeets, R. M.; Keyser, U. F.; Dekker, N. H.; Dekker, C. Noise in Solid-State Nanopores. *Proc. Natl. Acad. Sci. U. S. A.* **2008**, *105*, 417–421.
34. Hooge, F. N.  $1/f$  Noise Is No Surface Effect. *Phys. Lett. A* **1969**, *29*, 139–140.
35. Dekker, R. M. M. S. and N. H. D. and C. Low-Frequency Noise in Solid-State Nanopores. *Nanotechnology* **2009**, *20*, 95501.
36. Larkin, J.; Foquet, M.; Turner, S. W.; Korlach, J.; Wanunu, M. Reversible Positioning of Single Molecules inside Zero-Mode Waveguides. *Nano Lett.* **2014**, *14*, 6023–6029.
37. Smeets, R. M.; Keyser, U. F.; Krapf, D.; Wu, M. Y.; Dekker, N. H.; Dekker, C. Salt Dependence of Ion Transport and DNA Translocation through Solid-State Nanopores. *Nano Lett.* **2006**, *6*, 89–95.
38. Kraus, J. D. *Electromagnetics*; Carver, K. R., Ed.; McGraw-Hill electrical and electronic engineering series; McGraw-Hill: New York, 1973.
39. Zhu, P.; Craighead, H. G. Zero-Mode Waveguides for Single-Molecule Analysis. *Annu. Rev. Biophys.* **2012**, *41*, 269–293.
40. Aksimentiev, A.; Heng, J. B.; Timp, G.; Schulten, K. Microscopic Kinetics of DNA Translocation through Synthetic Nanopores. *Biophys. J.* **2004**, *87*, 2086–2097.

41. Heng, J. B.; Ho, C.; Kim, T.; Timp, R.; Aksimentiev, A.; Grinkova, Y. V.; Sligar, S.; Schulten, K.; Timp, G. Sizing DNA Using a Nanometer-Diameter Pore. *Biophys. J.* **2004**, *87*, 2905–2911.
42. Liu, H.; Qian, S.; Bau, H. H. The Effect of Translocating Cylindrical Particles on the Ionic Current through a Nanopore. *Biophys. J.* **2014**, *92*, 1164–1177.
43. Menestrina, J.; Yang, C.; Schiel, M.; Vlassiouk, I.; Siwy, Z. S. Charged Particles Modulate Local Ionic Concentrations and Cause Formation of Positive Peaks in Resistive-Pulse-Based Detection. *J. Phys. Chem. C* **2014**, *118*, 2391–2398.
44. Ling, D. Y.; Ling, X. S. On the Distribution of DNA Translocation Times in Solid-State Nanopores: An Analysis Using Schrödinger's First-Passage-Time Theory. *J. Phys. Condens. Matter* **2013**, *25*, 375102.
45. Jonsson, M. P.; Dekker, C. Plasmonic Nanopore for Electrical Profiling of Optical Intensity Landscapes. **2013**, 8–12.
46. Jothimuthu, P.; Carroll, A.; Bhagat, A. A. S.; Lin, G.; Mark, J. E.; Papautsky, I. Photodefinable PDMS Thin Films for Microfabrication Applications. *J. Micromechanics Microengineering* **2009**, *19*, 45024.
47. Rosenstein, J. K.; Wanunu, M.; Merchant, C. a; Drndic, M.; Shepard, K. L. Integrated Nanopore Sensing Platform with Sub-Microsecond Temporal Resolution. *Nat. Methods* **2012**, *9*, 487–492.
48. Eilers, P. H. C.; Boelens, H. F. M. Baseline Correction with Asymmetric Least Squares Smoothing. *Leiden Univ. Med. Cent. Rep.* **2005**.

